Proceedings of the 1st Global Power and Propulsion Forum
GPPF 2017
Jan 16-18, 2017, Zurich, Switzerland
www.pps.global

GPPF-2017-22

A THREE-DIMENSIONAL FLUID-STRUCTURE-THERMAL SIMULATION OF BUMP-TYPE FOIL THRUST BEARINGS

Kan Qin
Queensland Geothermal Energy Centre of Excellence, School of Mechanical and Mining Engineering, The University of Queensland
k.qin1@uq.edu.au
Brisbane, QLD, Australia

Peter A. Jacobs
Queensland Geothermal Energy Centre of Excellence, School of Mechanical and Mining Engineering, The University of Queensland
p.jacobs@uq.edu.au
Brisbane, QLD, Australia

Joshua Keep
Queensland Geothermal Energy Centre of Excellence, School of Mechanical and Mining Engineering, The University of Queensland
j.keep@uq.edu.au
Brisbane, QLD, Australia

Ingo H. Jahn
Centre for Hypersonics, School of Mechanical and Mining Engineering, The University of Queensland
i.jahn@uq.edu.au
Brisbane, QLD, Australia

ABSTRACT

Foil bearings are a promising technology that enables high-speed turbomachinery systems. Applications include air cycle machines and turbomachinery for supercritical CO_2 cycles. As operating conditions become more challenging, the demand for more comprehensive models to simulate foil thrust bearings has grown. This paper presents a multi-physics multi-timescale computational framework for the three-dimensional and two-way coupled fluid-structure-thermal simulation of foil thrust bearings. Individual solvers for the transient fluid flow, structural deformation and heat conduction as well as the coupling strategy are discussed. Next, heat transfer models of the solid structures within foil thrust bearings are also described in detail. The result is a multi-physics computational framework that can predict the steady state and dynamic performance of foil thrust bearings. Numerical simulations of foil thrust bearings with air and CO_2 are performed using this framework and new insight into the operation of foil bearings with CO_2 is discussed.

INTRODUCTION

The supercritical Carbon Dioxide (sCO_2) cycle is considered as a potential alternative to conventional steam power cycle with the advantages of higher efficiency and compact turbomachinery systems [1]. However, many challenges have to be overcome before this cycle can be realised, because CO_2 exhibits different behaviours when compared to air or steam. The key components of the supercritical CO_2 cycle have been actively studied in recent years. For example, foil bearings (journal and thrust) were tested at Sandia National Laboratories to demonstrate a higher efficiency and more efficient operation of supercritical CO_2 cycles compared to using alternative conventional ball bearings. Typical foil bearings are bump-

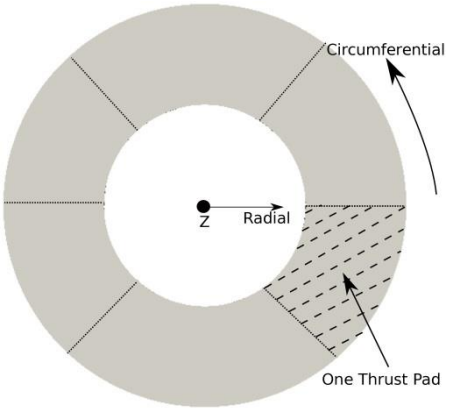

(a) **Top view**.

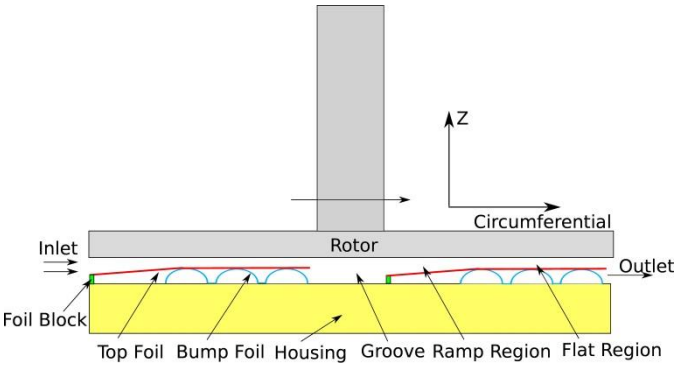

(b) **Side view.**

Fig. 1: Schematic diagram of foil thrust bearings.

This work is licensed under a Creative Commons Attribution 4.0 International License Creative Commons Attribution-NonCommercial-NoDerivatives 4.0 International License

type, which are composed of a top foil and a corrugated bump foil. The top foil is affixed to the bearing housing or a foil block on the upstream side, and on the downstream side, it sits at the height of its bump under structure. This forms a partially ramped profile as indicated in Fig. 1.

The film height (the clearance between rotor and top foil) in the ramp region can be adjusted by implementing a foil block. The use of foil bearings in high-speed turbomachinery systems has various advantages compared to rolling element bearings. The favourable characteristics of foil bearings are improved reliability, elimination of lubricant oil supply system, operation capability at very high and low temperatures, improved dynamic characteristics, tolerance to minor shaft misalignment and external perturbations and the low viscosity of the gas working fluid resulting in lower power losses.

While there are many inherent advantages to foil bearings, there are several limitations. The most important problems during experiments at high speed are high local temperature gradients, which cause thermal runaway of foil bearings [2]. This is due to the weak conduction rate of the thin foil structure and low heat capacity of air. The small contact areas between top foil and bump foils and low heat capacity prevent conductive heat removal from the fluid flow. Hence, the temperature distribution within foil bearings has to be carefully considered in design, particularly for bearings operated with high rotational speed or high load.

Salehi et. al. [3] performed the first study to model and characterise thermal properties of gas foil journal bearings. The Couette flow approximation to the energy equation was implemented with the compressible Reynolds equation. This simplified method provided a reasonable agreement with experimental data, but with a maximum over-prediction of 19%. Sim and Kim [4] presented a thermo-hydrodynamic model that accounted for the thermal contact resistance between the top foil, bump foil and bearings housing. The mixing effect between the leading and trailing edges of top foils was also investigated. The suction flow mixing ratio at the groove region was obtained and then applied to their developed model. The detailed mixing model in the groove region is outlined in Ref. [5]. The proposed cooling strategy was to radially supply flow into the mixing zone. The feasibility of the radial injection cooling had been experimentally tested by Shrestha et al. [6]. In addition, the heat conduction behaviour from the top foil to the back plate via the bump foil was experimentally determined in Ref. [7].

The aforementioned work is for the thermo-hydrodynamic modelling of foil journal bearings. Little work had been undertaken to model the temperature field for foil thrust bearings. The Couette flow approximation of the energy equation from Salehi et. al. [3] was also implemented by Gad and Kaneko [8] to predict the temperature distribution for air foil thrust bearings. But a validation case was missing due to the lack of experimental data for foil thrust bearings. Lee and Kim [9] proposed a three-dimensional thermo-hydrodynamic analysis of Raleigh step air foil thrust bearings with a forced cooling air flow and the optimum cooling air pressure was found based on the reference simulation condition. For air foil thrust bearings, the influence of temperature rise on the bearing performance was not significant. San Andrés and Ryu [10] conducted isothermal simulations which matched well with the experimental data.

For CO_2 foil thrust bearings, the operating fluid is far more dense than air, less viscous compared to oil, and highly non-ideal. These factors present challenges when predicting the performance of foil bearings. This includes the potential for turbulent flow, highly compressible flow, non-linear thermodynamic properties and non-negligible centrifugal inertia force due to high density and high-speed operation. These challenges have been numerically confirmed by Qin et. al. [11, 12] and it was found that Reynolds equation is not adequate to model fluid flow of CO_2 foil thrust bearings. Another challenge for CO_2 foil thrust bearings is the viscous heating effect. Due to high speed operation, turbulent flow regime and reduced heat conducting area of the bump foil structure, temperatures within foil bearings can be significant, and exceed the temperature limit of materials. The turbulent thermo-elastohydrodynamic analyses of hybrid thrust bearings and journal bearings with CO_2 as the operating fluid has been conducted by Xu et. al. [13] and Kim [14]. A high temperature increase is observed in their simulations. A numerical thermo-elastohydrodynamic analysis of a novel radial foil thrust bearings has been reported by Lee and Kim [9]. At a rotational speed of 50000rpm and a load of 200N, the maximum temperature rise is approximately 70K for a case where cooling flow is prescribed. However, for typical foil journal or thrust bearings, there is no pressure gradient between the inner and outer radii, which results in no forced cooling flow through the bump foils. Thus the temperature increase in typical foil bearings, recirculating coolant by natural pumping, can be much higher than the value reported in [9]. In this case, the thermal effect on the performance of foil thrust bearings should be considered.

In addition to modelling challenges for CO_2 foil thrust bearings, supercritical CO_2 turbomachinery experiences much higher thrust loads due to high absolute pressure and pressure difference across the turbine and compressor. For example, a prototype sCO2 turbine-compressor with a compressor diameter of 18 mm, tested by Sandia National Laboratories generated an axial thrust load of 533 N at the rotational speed of 30000 rpm [2]. Similarly a prototype 100 kW turbine concept developed at the author's institute requires a thrust bearing capacity of greater than 1000 N.

This paper presents a computational framework for a three-dimensional fluid-structure-thermal simulation of foil thrust bearings. The in-house CFD code Eilmer [15] is used to simulate fluid flow within foil thrust bearings in three dimensions. A two dimensional thin plate theory is applied to solve the structural deformation of the top foil and bump foils are modelled as a spring-like structure [16]. LaplacianFoam from FOAM-extend-3.0 toolbox is selected as the heat conduction solver [17].

The paper is organised as follows. First, the basic computational framework for fluid-structure-thermal

simulations is provided including a description of the fluid, structural deformation, and heat conduction solvers. Next, the coupling strategies between these solvers are introduced. The specific heat transfer model applied for foil thrust bearings is then detailed. Finally, the fluid-structure-thermal simulation results for air and CO_2 foil thrust bearings are presented.

COMPUTATIONAL MODEL

The computational model includes three aspects: fluid, structural deformation, and heat conduction solvers. The in-house CFD code Eilmer is used as the fluid solver [15] as both the steady state and dynamic performances of foil thrust bearings are of interest. A two-dimensional solver is also used to model the structural deformation of the top foil [16]. The bump foils are modelled as a spring-like structure and the stiffness is calculated based on the method from Gad et al. [18]. This approach considers interaction between bumps and the friction between the bump foil and the surrounding structure. Since the fluid and structural deformation solvers and their coupling method have been detailed in Ref. [15, 16, 19]. Only the heat conduction solver LaplacianFoam is explained.

Heat Conduction Solver

As the fluid solver Eilmer currently is not capable of three-dimensional heat conduction analysis, the solver LaplacianFoam from the open source CFD toolbox FOAM-Extend-3.0 is used to model heat conduction through solid parts of the foil bearings. The governing equation for conduction in LaplacianFoam is written as

$$\frac{\partial T}{\partial t} - \nabla^2 \left(D_T \cdot T \right) = 0 . \qquad (1)$$

where D_T is diffusivity of solid materials. Since LaplacianFoam is already a mature solver for solving the transient Laplace's equation, verification or validation cases are not provided here [20].

Coupling Method: Fluid-Thermal

For fluid-thermal interactions, only the steady-state performance of the foil thrust bearings is of interest due to the large time constant τ_{heat} for the heat conduction problem. At the final, steady state, the balance of the heat flux from each domain (fluid and solid) and the match of the temperature at the fluid-thermal interfaces are satisfied. The condition at the interface i can be mathematically expressed as

$$\mathbf{q}_{i,f} = \mathbf{q}_{i,\mathrm{s}} \qquad \mathbf{T}_{i,f} = \mathbf{T}_{i,\mathrm{s}} . \qquad (2)$$

Where $\mathbf{q}$ is heat flux, $\mathbf{T}$ is the temperature and subscripts f and s indicate the interface at the fluid and solid domain, respectively. Considering only conduction at the interfaces, the flux condition is expanded as

$$-\lambda_{i,f} \left. \frac{\partial \mathbf{T}}{\partial \mathbf{n}} \right|_{i.f} \cdot \mathbf{n}_i = -\lambda_{i,\mathrm{s}} \left. \frac{\partial \mathbf{T}}{\partial \mathbf{n}} \right|_{i.\mathrm{s}} \cdot \mathbf{n}_i . \qquad (3)$$

where λ is thermal conductivity. The spatial derivative, $\left. \frac{\partial \mathbf{T}}{\partial \mathbf{n}} \right|_{i.f}$, for the fluid domain is approximated using a one-sided difference between the wall-adjacent cell centre temperature and the interface temperature. The temperature gradient at the solid domain, $\left. \frac{\partial \mathbf{T}}{\partial \mathbf{n}} \right|_{i.\mathrm{s}}$, is defined as

$$\left. \frac{\partial \mathbf{T}}{\partial \mathbf{n}} \right|_{i.\mathrm{s}} = \frac{\mathbf{q}_{i,f}}{\lambda_{i,s}} . \qquad (4)$$

Since only the steady state of the foil thrust bearings is considered, a weakly coupled strategy is proposed for the fluid-thermal simulations. Relaxation at each iteration is necessary to increase the stability of the numerical scheme. A simple relaxation strategy is given by

$$\mathbf{T}_{i,f}^{k+1} = \mathbf{T}_{i,f}^{k} + \beta \mathbf{f}_{i,\mathrm{s}}^{k} . \qquad (5)$$

Where β is the under-relaxation factor and k is the index of the iteration loop. During the iteration loop k, the nonlinear operation is applied to an input vector $\mathbf{T}_{i,f}^{k}$ generating an output vector $\mathbf{T}_{i,\mathrm{s}}^{k}$ of the same size. The residual vector is defined as $\mathbf{f}^{k} = \mathbf{T}_{i,\mathrm{s}}^{k} - \mathbf{T}_{i,\mathrm{f}}^{k}$. Typically β is set to a constant $0<\beta<1$. This relaxation factor is consistent for each cell but different at each fluid-thermal time step.

Alternatively, an optimal value of the relaxation factor can be selected in each iteration. Different dynamic relaxation techniques are reported in literature. In this study, we use the variant of vector Aitken Δ^2 method formulated in Ref. [21], because it is easy to be implemented and does not require too much memory during computations. This algorithm starts with a known sequence of two input/output pairs of vectors and calculates an optimum relaxation parameter as

$$\beta_k = \beta_{k-1} + \beta_{k-1} \frac{\Delta \mathbf{f}^{k^T} \mathbf{f}^{k}}{\left\| \mathbf{f}^{k} \right\|_2^2} . \qquad (6)$$

With the residual difference vector $\Delta \mathbf{f}^{k} = \mathbf{f}^{k-1} - \mathbf{f}^{k}$. The first iteration is carried out using a pre-selected relaxation constant β_0. This method is straightforward to implement, needs minimum processor and storage resources, only taking a single residual evaluation per iteration. The entire procedure is outlined as follows

1. The fluid domain is solved by Eilmer with an imposed initial temperature $\mathbf{T}_{i,f}^{k}$ until an equilibrium fluid state condition is achieved;
2. Heat flux $\mathbf{q}$ at the fluid-solid interfaces is extracted from Eilmer. The temperature gradient $\left. \frac{\partial \mathbf{T}}{\partial \mathbf{n}} \right|_{i.s}$ at the solid side is calculated based on the continuity of heat flux across the fluid-structure boundary (Eqn. 4);
3. The temperature gradient $\left. \frac{\partial \mathbf{T}}{\partial \mathbf{n}} \right|_{i.s}$ is taken as the boundary condition for the heat conduction analysis. The simulation is conducted with LaplacianFoam until the temperature solution in the solid is converged;

4. The surface temperature $\mathbf{T}_{i,s}^{k}$ at the interfaces from LaplacianFoam is extracted. The new $\mathbf{T}_{i,f}^{k+1}$ is determined as the boundary condition for Eilmer. In the first iteration loop, a pre-defined under-relaxation factor is used in Eqn. 5, otherwise β is calculated with Eqn. 6.

5. Repeat steps 1-4 using the new $\mathbf{T}_{i,f}^{k+1}$ until convergence. For air foil thrust bearings, it typically takes 60 iteration loops, while 30 loops are needed for CO_2 foil thrust bearings.

The validation of the proposed fluid-thermal coupling method is shown in Appendix.

Coupling Method: Fluid-Structure-Thermal

The three individual solvers for the current problem (transient fluid flow, structural deformation and heat conduction) within foil thrust bearings have been described as well as the individual coupling methods for fluid-structure and fluid-thermal simulations. However, these solvers have to be coupled for a full fluid-structure-thermal simulation, which involves fluid-structure, fluid-thermal and structure-thermal simulations. The magnitude of the structural deflection is typically in microns, thus the effect of the deflection is minimal when solving the heat diffusion problem in the solid. Therefore, the coupling between the structure and thermal solvers is ignored.

The schematic diagram for the fluid-structure-thermal simulations is shown in Fig. 2 including information exchange between the solvers. A tight coupling is implemented between the fluid and structure solvers, as the structural deformation reacts to the pressure increase in the fluid domain quickly. Transient simulations of the coupled fluid-structure system, starting from stationary fluid case, have shown that the dynamically coupled fluid structure system can reach a steady operating point in less than 1 ms. However, as noted prior, the time constant in the heat conduction solver is large, usually of the order of minutes. The temperature field takes a long time to achieve the equilibrium state. As shown in Ref. [6], it usually takes 3000 s for a three-pad journal bearings to reach the thermal equilibrium state. Hence, a weak coupling between the fluid and heat conduction solvers is selected.

The coupling method for the fluid-structure-thermal simulation is almost the same as the fluid-thermal simulation: the only difference is the closely coupled fluid-structure problem is simulated together in step 1. As the time constant for the heat conduction problem is large compared to that of the fluid-structure simulations, there is no need to consider the temperature variation of the structural part when investigating the transient behaviour of the fluid structure interactions.

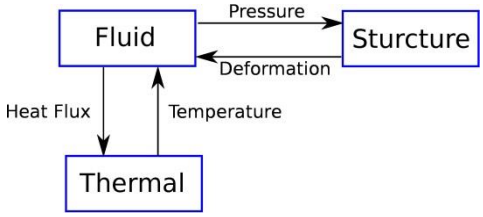

Fig. 2:Computational framework.

APPLICATION TO FOIL THRUST BEARINGS

In this section, the detailed analysis using the above computational tool for foil thrust bearings is described. The layout of a foil thrust bearings in a typical turbomachinery system is shown in Fig. 3. It consists of shaft, rotor, stator (bump and top foils) and bearing housing. In the current analysis, the simulation domain is extended to include the rotor, stator and housing to allow a full fluid-structure-thermal simulation of foil thrust bearings. This provides an accurate temperature distribution within the foil thrust bearings.

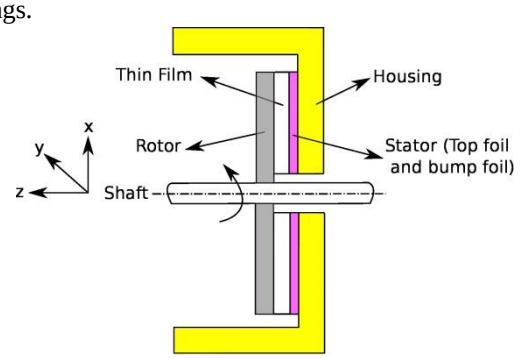

Fig. 3: Schematic diagram of the layout of foil thrust bearings.

Heat Transfer Model for Rotor

The computational domain of the rotor is depicted in Fig. 4, where a computational mesh of 64 × 120 × 40 is used. Although foil thrust bearings consist of several sectors (usually 6), only one sector is simulated with the periodic boundary condition to reduce the computational cost. The computational domain for the rotor is a slightly different from that of the thin film. The inner radius is extended to the shaft as shown in Fig. 8, but the outer radius is the same as the fluid domain.

For boundary conditions, the north and south boundaries (shaded surfaces) are connected with periodic boundary conditions. The bottom boundary ($z = z_{\min}$) is modelled as the fluid-solid interface, and the coupling method for fluid-thermal simulation is used at this surface. However, as the rotor is spinning, mixing-plane theory is applied when mapping the heat flux from fluid domain to the rotor. In this way, heat flux at the fluid domain is averaged in the tangential direction when passed to the solid interface. Since the west boundary (the inner radius) is connected with the shaft, a fixed operating temperature is imposed by considering the very large heat transfer area between the shaft and the operating fluid. At the east (the outer radius) and top ($z = z_{\max}$) surfaces, convective heat transfer is assumed, in accordance with a simple rotating disk exposed to an infinite quiescent medium. The following empirical correlations for local heat transfer in a flow induced by a rotating disk in terms of the local Reynolds number, Re_r [22] are used, where the outer radius is used as the characteristic length.

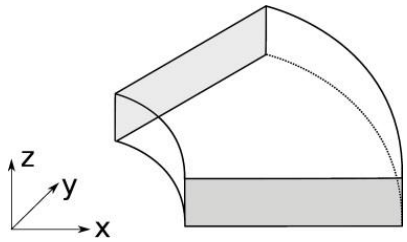

Fig. 4: Computational domain of rotor.

$$Nu = 0.33\,\mathrm{Re}^{0.5}\,\mathrm{Pr}^{1/3} \qquad \mathrm{Re}_r < 1.95\times10^5$$
$$Nu = 10\times10^{-20}\,\mathrm{Re}^{4}\,\mathrm{Pr}^{1/3} \quad 1.95\times10^5 < \mathrm{Re}_r < 2.5\times10^5 \quad (7)$$
$$Nu = 0.0188\,\mathrm{Re}^{0.8}\,\mathrm{Pr}^{1/3} \qquad \mathrm{Re}_r > 2.5\times10^5$$

Heat Transfer Model for Stator

The computational domain of the stator is shown in Fig. 5. The stator geometry is much more complex than the rotor, and consists of top foil, bump foil and housing.

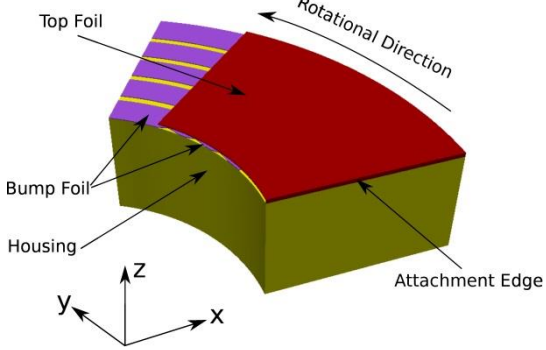

(a) Stator in three-dimensions.

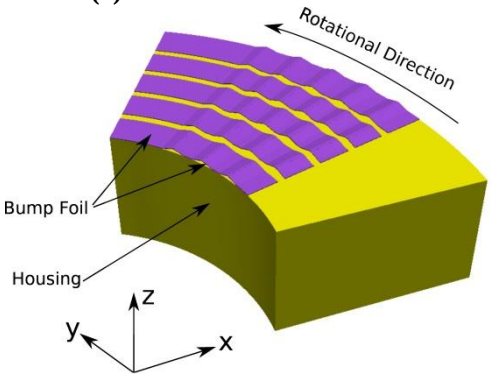

(b) Stator with top foil removed.

Fig. 5: Computational domain of stator.

The upper surface of the top foil is the fluid-thermal interface, and the coupling method for fluid-thermal simulation is implemented at this boundary. Since the stator is a non-rotating part, and as there is a slight pressure difference in the radial direction, a natural convective boundary condition is approximated at the inner and outer radius, within the bump foil channels and on the backside of the top foil [7]. In typical foil bearing applications, the forced convective cooling, achieved through a pressure gradient between the bearing inner and outer edge, is employed to cool the rear of the top foil and bump foil structure. The pressure gradient is a parameter that is set to suit the application (rotational speed and load). To remove the additional dependency on pressure gradient, the current study employs natural convection through the bump channel, rear of top foils, and inner and outer surfaces of the housing. The heat transfer coefficients are calculated as per the method described in [23]

$$Nu = 0.36 + \frac{0.518\left(Gr\,\mathrm{Pr}\right)^{1/4}}{\left(1+\left(0.559/\mathrm{Pr}\right)^{9/16}\right)^{4/9}} \qquad Gr\,\mathrm{Pr} < 10^9 . \quad (8)$$

where Gr is the Grashof number, Pr is the Prandtl number and Nu is the Nusselt number. However, the presented modelling framework has the flexibility to incorporate a forced convection model, as required.

In addition, the back surface of the top foil and the stator housing experience thermal and mechanical contact with the bump foil. Fig. 6 illustrates the thermal resistances at the bump contacts with the top foil and bearing housing. The bump foil links the temperature fields, which is dominated by the thin film, to the bearing housing via these thermal contact resistances. Thermal contacts are quite complicated in nature due to the thermal constriction and spreading of heat flux lines as well as the random distribution and the unknown boundary condition of micro-contacts [4]. Among several corrections for nominally flat rough surfaces, the thermal contact resistance (m^2K/W) obtained from experimental results in [7, 9] is used.

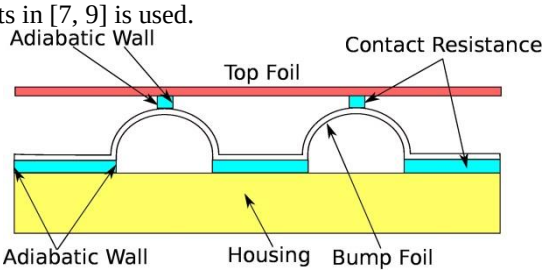

Fig. 6: Schematic diagram of heat transfer from top foil to thrust plate.

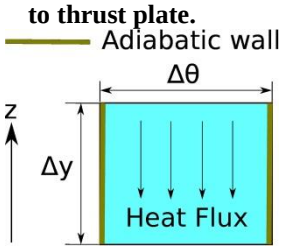

Fig. 7: Schematic diagram of the additional structure to account for the contact resistance.

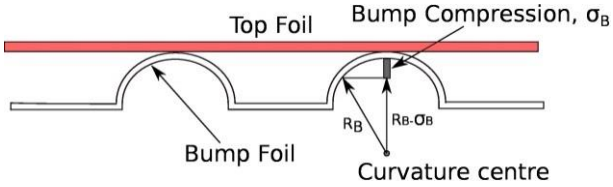

Fig. 8: Schematic diagram of the deflection of bump foil.

$$R_{cont} = (7.115\,\mathrm{P}_{bump}^4 - 16.159\,\mathrm{P}_{bump}^3 + 13.08\,\mathrm{P}_{bump}^2 - 4.503\,\mathrm{P}_{bump} + 1.207)\times10^{-3} \quad \mathrm{P}_{bump} <= 0.9 \quad (11)$$
$$R_{cont} = 0.633\times10^{-3} \quad \mathrm{P}_{bump} > 0.9$$

where P_{bump} is the local gauge pressure expressed in bar. For the present study, these contact resistances are modelled as additional structures within the foil thrust bearings as shown in Fig. 7. For these additions, boundaries that are not connected with the top foil or bump foil or housing are modelled as adiabatic walls as shown in Fig. 6. The height of the additional structure Δy is calculated as

$$\Delta y = \lambda_s R_{cont} . \qquad (12)$$

The bump contact area (A_{cont}) to the top foil varies depending on the applied pressure and is accompanied by beam-like deformation of the top and bump foils, as illustrated in Fig. 8. For simplicity, the bump contact area is approximated using the model shown in Fig. 8. Using the top foil deflections due to the applied pressure, the contact distance for a half bump arc is determined by the horizontal length calculated by the trigonometric relation to the bump radius. The bump foil deflection σ_B is obtained from the fluid-structure simulation. The trigonometric relation shown in Fig. 8 determines the contact distance using the bump arc radius of curvature (R_B) and the calculated bump foil deflection, resulting in contact width:

$$\Delta\theta = 2\sqrt{R_B^2 - \left(R_B - \sigma_B\right)^2} . (13)$$

RESULTS AND DISCUSSION

Table 1: Geometry of foil thrust bearings.

Number of pads	6
Outer diameter	101.6 mm
Inner diameter	50.8 mm
Shaft diameter[a]	46 mm
Pad arc extend	45 deg
Pad tapper extend	15 deg
Groove extend	60 deg
Top foil thickness	0.15 mm
Rotor thickness[a]	16 mm
Stator thickness[a]	20 mm
Groove depth[a]	0.6 mm
Rotation speed	21 krpm
Pad area	6080.5 mm^2
Working fluid	air and CO_2
Operating condition, air	0.1 MPa and 300 K
Operating condition, CO_2	1.4 MPa and 300 K
Initial min. film thickness	10.12 μm (air) and 17.82 μm (CO_2)
Rotational Re number	73 (air) and 3533 (CO_2)
Load	110 N
Load per unit area	18.1 kPa
Power loss	47.94 W (air) and 146.51 W (CO_2)

The fluid domain is shown in Fig. 9. The computational mesh of $48 \times 96 \times 15$ is from previous studies [11]. It is recommended by Bruckner [24] that the groove between adjacent thrust pads be used for passive thermal control, hence this part is also modelled. The leading and trailing edges of a thrust pad are connected with cyclic boundary conditions. The stator geometry shown in Fig. 5 is meshed with an in-house tool and converted into an OpenFOAM format mesh [25]. The studied bearing geometry is in accordance with the bearing presented by NASA [26], summarised in Table 1. Not all data for this geometry is released by NASA, with parameters labelled with [a] estimated based on the authors' experience.

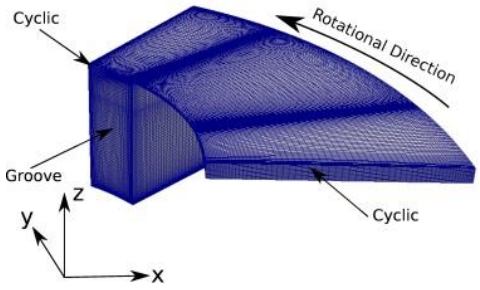

Fig. 9: Computational domain of foil thrust bearings, expanded in z direction.

To assess the relative performance of the bearing operating with air and CO_2, the bearing is simulated with an axial load of 110 N applied to the rotor. The remaining operating conditions are summarised in Table 1. At these conditions, the power loss is 47.94 W and 146.51 W for air and CO_2 respectively. The higher loss for CO_2 is attributed to this bearing operating in a turbulent flow regime [27]. The temperature distributions within the fluid, close to the fluid-structure interface are depicted in Fig. 10 and 11. The rotor temperatures are smeared circumferentially due to the rotor motion. At the same time there is an increase in temperature at the radial direction, due to increase in relative velocity and outward convection of the fluid. Contrary to this on the stator, a non-uniform temperature develops. This is due to better heat transfer from the rear of the top foil to the bump foils, compared to natural convection that is applied to the remainder of the top foil rear surface.

Experimental data for thrust bearing foil temperature distributions are limited. Furthermore, the thermal boundary condition and structural parameters of the rotor and stator are generally not provided. These parameters are essential for the thermal analysis and to thermally anchored simulations [7, 28]. Also, data in literature relates to journal style bearings (for example [29]), these have only limited value in regards to thrust bearings, which have substantially different rotor and stator shapes and boundary conditions. Therefore, verification and analysis relies on the investigation of energy conservation and flows.

Heat is generated within the thin gas film due to a combination of viscous effects and compression work on the fluid. This heat, which equals the power loss, can be removed by the following processes:

1. Advection by the gas being pumped through the film in the radial direction;
2. Convection into the rotor. Heat conducts through the rotor, either to the shaft (a fixed temperature boundary) or to the rear and outside surface, where forced convection takes place to an infinite fluid reservoir at 300 K;

3. Convection into the top foil. From here heat is removed either by natural convection within the bump foil structure (from top foil, bump foils and bearing housing) or conduction into the bearing housing through the bump foils. Boundary conditions are set at 300 K.

The net heat flowcharts for air and CO_2 are shown in Figs. 10 (c) and 11 (c). In both cases the majority of the heat is convected to the rotor (90% and 67% for air and CO_2). This is due to good thermal conductivity of the rotor, which is able to maintain a surface temperature substantially below the stator. Once heat enters the rotor, the split between conduction to shaft and convection on the rear surface is substantially different (see relative heat flux in Fig. 10 and 11). In the case of CO_2, the turbulent flow regime, provides a much higher heat transfer coefficient (2314 W/m^{2}K) on the rotor outside surface, approximately 10 times bigger than the corresponding coefficient for air (238 W/m^{2}K). These heat transfer coefficients, and corresponding surface temperature highlights the ability of CO_2 to provide effective heat removal through the rotor.

In contrast, the top foil surface reaches a significantly higher temperature and only a much smaller portion of the heat is convected in this direction. This is caused by the much higher thermal resistance of the bump foil structure. This is due to the contact resistance and also small conduction areas within the bump foils. Considering the split of heat flux downstream of the top foil, it can be seen that this is similar for the air and CO_2. The majority of heat (~88%) is conducted into the bearing housing structure. The remainder is convected to the fluid present within the bump channels. Most convection takes place from the top foil rear surface (~9%), followed by the bump foils (~2.5%), and a bit from the bearing housing surface (~0.3%). However, the total amount of removed energy is low because heat transfer relies on natural convection. These power splits within the bump channel are consistent with the results from Ref. [7].

A further aspect to consider is advection of heat by the gas in the film which is driven by the radial pumping of the bearing. The pumping mass flow rates are 0.004 g/s and 0.155 g/s for air and CO_2, respectively. The higher flow rate for CO_2 is caused by increased density and centrifugal effects as discussed in Refs. [10, 11]. With the increased radial mass flow, the CO_2 bearing is able to advect a substantially larger portion of the generated heat. Through this process, the CO_2 bearing is able to remove approximately 30% of the generated heat, whereas the air bearing is only capable of removing 3%. This illustrates the favourable impact of radial pumping on bearing cooling.

In future CO_2 applications, it is expected that foil thrust bearings will be required to operate with substantially higher loads due to the substantially higher operating pressures. While the comparison to air bearings has shown a favourable cooling performance, in particular due to the advection within in the film, more substantial cooling improvements will be required to maintain low, uniform top foil temperatures. A mechanism to achieve this is to force fluid through the bump channels, for example, by applying a

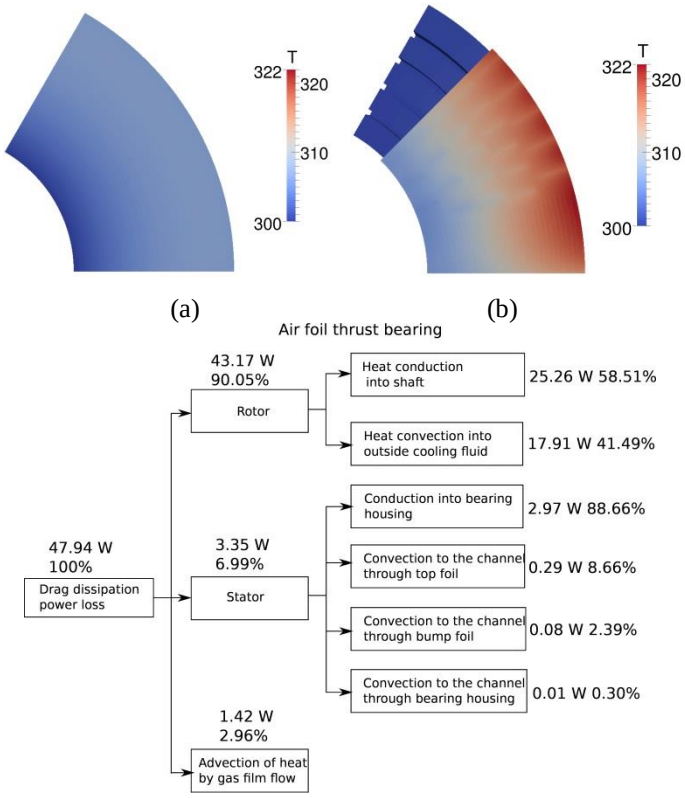

Fig. 10: Air foil thrust bearings interface temperatures: (a): rotor; (b): stator; (c): heat flowchart for complete bearing.

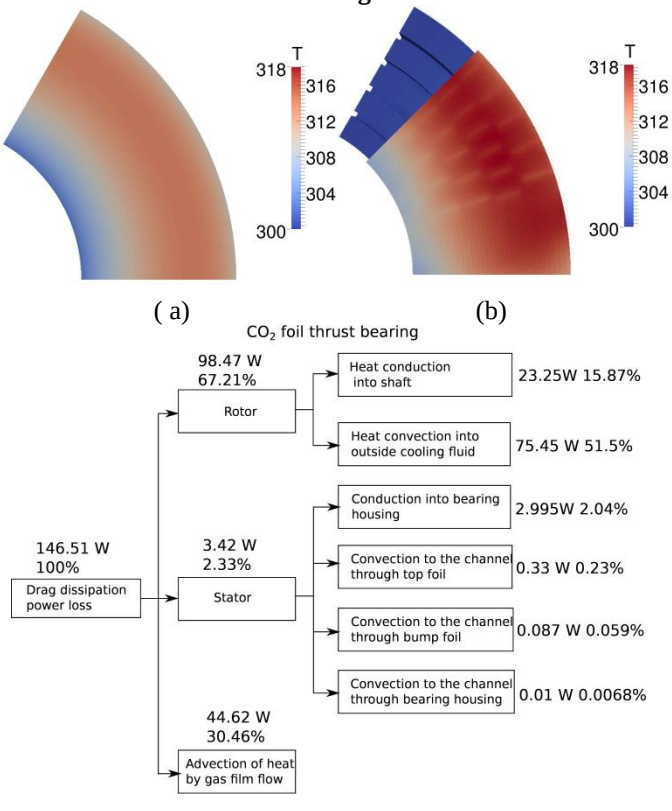

Fig. 11: CO_2 foil thrust bearings interface temperatures: (a): rotor; (b): stator; (c): heat flowchart heat flowchart for complete bearing.

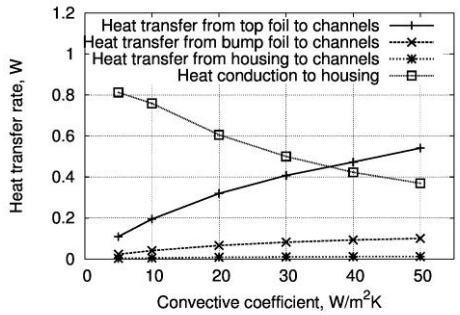

Fig. 12: Comparison of heat flow for different convection coefficients within the bump channels.

pressure difference in the radial direction. To provide insight towards this approach, a thermal investigation was conducted to analyse the effect of increasing heat transfer coefficient within the bump channels. For this analysis, only the stator side is considered. A uniform heat flux, corresponding to 1 W per pad (164 W/m^2), is applied to the fluid side of the top foil. The resulting distributions of heat flow for different convective coefficients are shown in Fig. 12. The lowest heat transfer coefficient of 5 W/m^{2}K corresponds to the natural convection coefficient used previously. These data show that increasing heat transfer in the bump channels is an effective way to extract a larger portion of the supplied heat directly from the rear of the top foil. At the same time, the requirement to conduct heat to the bearing housing through the bump foils diminishes.

CONCLUSION

In this paper, a computational framework for the fluid-structure-thermal simulations of foil thrust bearings is developed. Individual solvers and their coupling strategies are detailed together with validation cases. A detailed description of the implemented foil bearing heat transfer models is provided.

The numerical tool is used to conduct a comparative study between a foil thrust bearing of the same geometry operating with air and CO_2. This comparison highlights a number of differences in bearing operation, in particular the heat fluxes and cooling requirements. Key findings are:

1. Power loss and heat generation increases three-fold for the CO_2 bearing. However, due to improved cooling, peak temperatures are maintained below the air case.
2. The CO_2 bearing significantly benefits from increased convective cooling on the rear surface of the rotor. This allows substantially more energy to be extracted through the rotor.
3. Almost a third of the generated heat is advected with the fluid in the CO_2 case, compared to only 3% in the air case. This effect, caused by the centrifugal pumping that naturally occurs in CO_2 bearings due to the high fluid density [10, 11], provides a new and effective cooling mechanism for the CO_2 bearing.
4. Heat transfer to the stator is similar for both cases. Here heat flow is limited due to the high thermal resistance imposed by the bump structure. Only a comparatively small portion of the heat flux entering the top foil is extracted via convection to fluid in the bump channels when natural convection is assumed.
5. A separate numerical investigation showed that applying force convection in the bump channels is an effective approach to enhance cooling, which will be essential for bearings operating at high loads.

This work has provided some new insights to the heat flux distribution in foil bearings, how this is affected by the working fluid, and was identified mechanisms to enhance this heat transfer.

ACKNOWLEDGEMENT

This research was performed as part of the Australian Solar Thermal Research Initiative (ASTRI), a project supported by Australian Government. Kan Qin, would also like to thank China Scholarship Council, The University of Queensland and Queensland Geothermal Energy Centre of Excellence for their financial support. This work was supported by resources provided by The Pawsey Supercomputing Centre with funding from the Australian Government and the Government of Western Australia.

REFERENCES

1. Dostal, V., *A supercritical carbon dioxide cycle for next generation nuclear reactors*, 2004, Massachusetts Institute of Technology.
2. Wright, S.A., et al., *Operation and analysis of a supercritical CO_2 Brayton cycle.* Sandia Report, No. SAND2010-0171, 2010.
3. Salehi, M., E. Swanson, and H. Heshmat, *Thermal features of compliant foil bearings—theory and experiments.* Journal of Tribology, 2001. **123**(3): p. 566-571.
4. Sim, K. and T.H. Kim, *Thermohydrodynamic analysis of bump-type gas foil bearings using bump thermal contact and inlet flow mixing models.* Tribology International, 2012. **48**: p. 137-148.
5. Kim, D., et al., *Extended three-dimensional thermo-hydrodynamic model of radial foil bearing: case studies on thermal behaviors and dynamic characteristics in gas turbine simulator.* Journal of Engineering for Gas Turbines and Power, 2012. **134**(5): p. 052501.
6. Shrestha, S.K., D. Kim, and Y.C. Kim, *Experimental feasibility study of radial injection cooling of three-pad air foil bearings.* Journal of Tribology, 2013. **135**(4): p. 041703.
7. Lee, D. and D. Kim, *Thermohydrodynamic analyses of bump air foil bearings with detailed thermal model of foil structures and rotor.* Journal of Tribology, 2010. **132**(2): p. 021704.
8. Gad, A.M. and S. Kaneko, *Tailoring of the bearing stiffness to enhance the performance of gas-lubricated bump-type foil thrust bearing.* Proceedings of the Institution of Mechanical Engineers, Part J: Journal of Engineering Tribology, 2015: p. 1350650115606482.
9. Lee, D. and D. Kim, *Three-dimensional thermohydrodynamic analyses of Rayleigh step air*

foil thrust bearing with radially arranged bump foils. Tribology Transactions, 2011. **54**(3): p. 432-448.
10. San Andrés, L., K. Ryu, and P. Diemer, *Prediction of gas thrust foil bearing performance for oil-free automotive turbochargers.* Journal of Engineering for Gas Turbines and Power, 2015. **137**(3): p. 032502.
11. Qin, K., et al., *Development of a computational tool to simulate foil bearings for supercritical CO_2 cycles.* Journal of Engineering for Gas Turbines and Power, 2016. **138**(9): p. 092503.
12. Qin, K., I. Jahn, and P. Jacobs. *Effect of operating conditions on the elasto-hydrodynamic performance of foil thrust bearings for supercritical CO_2 cycles*. in *ASME Turbo Expo 2016*. 2016.
13. Xu, F. and D. Kim. *Three-dimensional turbulent thermo-elastohydrodynamic analyses of hybrid thrust foil bearings using real gas model*. in *ASME Turbo Expo 2016: Turbomachinery Technical Conference and Exposition*. 2016. American Society of Mechanical Engineers.
14. Kim, D., *Design space of foil bearings for closed-loop supercritical CO_2 power cycles based on three-dimensional thermohydrodynamic analyses.* Journal of Engineering for Gas Turbines and Power, 2016. **138**(3): p. 032504.
15. Gollan, R. and P. Jacobs, *About the formulation, verification and validation of the hypersonic flow solver Eilmer.* International Journal for Numerical Methods in Fluids, 2013. **73**(1): p. 19-57.
16. Qin, K. and I. Jahn, *Structural deformation of a circular thin plate with combinations of fixed and free edges.* Technical Report, School of Mechanical and Mining Engineering, 2015/05, 2015.
17. Weller, H.G., et al., *A tensorial approach to computational continuum mechanics using object-oriented techniques.* Computers in physics, 1998. **12**(6): p. 620-631.
18. Gad, A.M. and S. Kaneko, *A new structural stiffness model for bump-type foil bearings: application to generation ii gas lubricated foil thrust bearing.* Journal of Tribology, 2014. **136**(4): p. 041701.
19. Qin, K., I. Jahn, and P. Jacobs. *Development of a fluid-structure model for gas-lubricated bump-type foil thrust bearings.* in *Applied Mechanics and Materials*. 2016. **846**. p. 169-175.
20. Jasak, H., A. Jemcov, and Z. Tukovic. *OpenFOAM: A C++ library for complex physics simulations*. in *International workshop on coupled methods in numerical dynamics*. 2007. IUC Dubrovnik, Croatia.
21. Küttler, U. and W.A. Wall, *Fixed-point fluid–structure interaction solvers with dynamic relaxation.* Computational Mechanics, 2008. **43**(1): p. 61-72.
22. aus der Wiesche, S. and C. Helcig, *Convective heat transfer from rotating disks subjected to streams of air*. 2016: Springer.
23. Holman, J.P., *Heat transfer*. 10th ed.. ed. 2010, Boston: Boston : McGraw Hill Higher Education.
24. Bruckner, R., *Method to Increase Performance of Foil Bearings Through Passive Thermal Management.* 2013.
25. Jahn, I.H. and K. Qin, *e3prepToFoam: a mesh generator for OpenFOAM*. Technical Report, School of Mechanical and Mining Engineering, 2015/04, 2015.
26. Dykas, B., et al., *Design, fabrication, and performance of foil gas thrust bearings for microturbomachinery applications.* Journal of Engineering for Gas Turbines and Power, 2008. **131**(1): p. 012301-012301.
27. Brunetière, N.l., B. Tournerie, and J. Fre, *Influence of fluid flow regime on performances of non-contacting liquid face seals.* Journal of Tribology, 2002. **124**(3): p. 515-523.
28. San Andrés, L. and T.H. Kim, *Thermohydrodynamic analysis of bump type gas foil bearings: a model anchored to test data*. Journal of Engineering for Gas Turbines and Power, 2010. **132**(4): p. 042504.
29. Radil, K. and M. Zeszotek, *An experimental investigation into the temperature profile of a compliant foil air bearing.* Tribology Transactions, 2004. **47**(4): p. 470-479.
30. Malatip, A., N. Wansophark, and P. Dechaumphai, *Combined streamline upwind petrov galerkin method and segregated finite element algorithm for conjugate heat transfer problems.* Journal of mechanical Science and Technology, 2006. **20**(10): p. 1741-1752.
31. Back, L., P. Massier, and H. Gier, *Convective heat transfer in a convergent-divergent nozzle.* International Journal of Heat and Mass Transfer, 1964. **7**(5): p. 549-568.
32. Marineau, E.C., J.A. Schetz, and R.E. Neel, *Turbulent Navier-Stokes simulations of heat transfer with complex wall temperature variations.* Journal of Thermophysics and Heat Transfer, 2007. **21**(3): p. 525-535.
33. Wilcox, D.C., *Formulation of the k-w turbulence model revisited.* AIAA journal, 2008. **46**(11): p. 2823-2838.

APPENDIX – Validation Cases

The fluid-thermal simulation is verified and validated with two test cases. The first test case is conjugate Couette flow between parallel walls. This is a typical shear driven flow for conjugate heat transfer analysis. The schematic diagram is depicted in Fig. 12 with a fluid bounded by a hot upper wall (with temperature T_0) that moves at a constant velocity and a stationary conducting solid. The side of the conducting solid away from the fluid is maintained at a constant temperature T_1. The left and right surfaces are connected with the periodic boundary condition. The solid part has a height of 0.25 m, while the height for fluid domain is 0.5 m. The dimensions for this conjugate Couette flow may be far larger than any engineering foil bearings,

however, that does not influence the correction of the theoretical result.

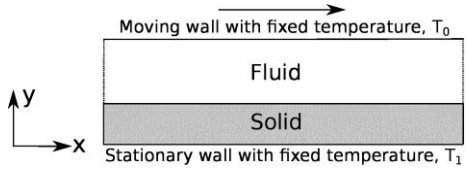

Fig. 12: Schematic diagram of conjugate Couette flow.

The temperature between the two parallel walls is extracted and compared for conducting ratios, $K = \lambda_s / \lambda_f$. The computed solutions are compared with the analytical solutions [30] in Fig. 13. This shows excellent agreement with the analytical solutions for two conducting ratios, 0.1 and 10. The relative error between numerical results and analytical solution is less than 0.04%.

The second test case (conjugate nozzle flow) is used to validate turbulent conjugate heat transfer. The supersonic flow inside a cooled axisymmetric convergent divergent nozzle is investigated. The analysis is based on the experimental data reported by Back et. al. [31]. The test nozzle is axisymmetric, has a throat diameter of 0.0458 m, and contraction area ratio of 7.75:1, and expansion area ratio of 2.68:1, a convergent half-angle of 30 deg, and a divergent half-angle of 15 deg. The detailed geometry and operating condition can be seen in Ref. [32].

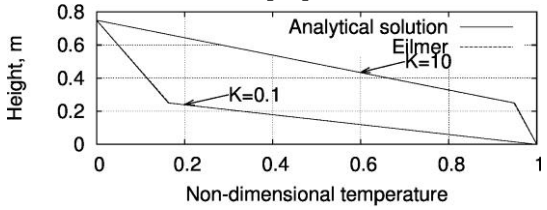

Fig. 13: Comparison of temperature distribution between fluid-thermal simulation and analytical solution.

The temperature distribution for the outer wall of the nozzle from the experiment is shown in Fig. 14(a). This is used as the non-uniform temperature boundary for the outer wall in the heat conduction simulation. The uncertainty on the temperature measurements is approximately 2% [31]. The inflow condition for this axisymmetric nozzle is a total temperature of 843.3K and a total pressure of 517.1kPa. This case of conjugate nozzle flow has previously been simulated by Marineau et al. [32]. The wall material was not specified by Back et al. [31], however the thermal conductivity of the material can be determined from the temperature gradient and the heat flux provided by Back et al. [31]. Marineau et al. [32] concluded that the thermal conductivity of the nozzle wall material is approximately 27W/mK. The conjugate nozzle heat transfer problem is solved by imposing the temperature from Fig. 14(a). at the outside wall. The temperatures at the solid sides that correspond to the nozzle inlet and outlet are specified as 299 and 283 K, respectively, as suggested by the experimental data. Turbulence was modelled using the Wilcox k-w model [33].

Fig. 14(b) shows the comparison between predicted inner wall temperatures and experimental data. The predicted wall temperatures are close to the experimental values. Due to unknown parameters from the experiment, there are some deviations between numerical results and experiment data, especially close to nozzle inlet and exit. This is also reported in Ref. [32]. This confirms the suitability of the proposed coupling strategy for fluid-thermal simulation.

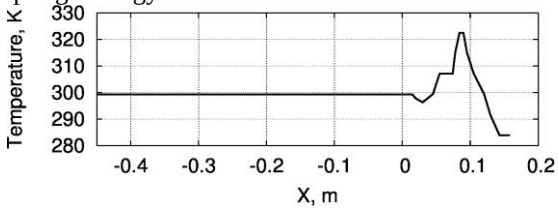

(a)

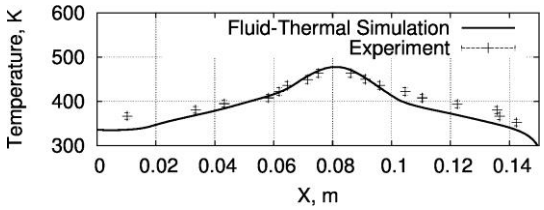

(b)

Fig. 14: (a) Temperature distribution along nozzle outer wall, (b) Comparison of temperature distribution along nozzle inner wall.